Constraining the S factor of ^{15}N$(p,\gamma)^{16}$O at astrophysical energies

P. J. LeBlanc,[1,*] G. Imbriani,[1,2,3] J. Görres,[1] M. Junker,[3] R. Azuma,[1,4] M. Beard,[1] D. Bemmerer,[5] A. Best,[1] C. Broggini,[6] A. Caciolli,[7] P. Corvisiero,[8] H. Costantini,[8] M. Couder,[1] R. deBoer,[1] Z. Elekes,[9] S. Falahat,[1,10] A. Formicola,[3] Zs. Fülöp,[9] G. Gervino,[11] A. Guglielmetti,[12] C. Gustavino,[3] Gy. Gyürky,[9] F. Käppeler,[13] A. Kontos,[1] R. Kuntz,[14] H. Leiste,[15] A. Lemut,[8] Q. Li,[1] B. Limata,[2] M. Marta,[5] C. Mazzocchi,[12] R. Menegazzo,[6] S. O'Brien,[1] A. Palumbo,[1] P. Prati,[8] V. Roca,[2] C. Rolfs,[14] C. Rossi Alvarez,[6] E. Somorjai,[9] E. Stech,[1] O. Straniero,[16] F. Strieder,[14] W. Tan,[1] F. Terrasi,[17] H. P. Trautvetter,[14] E. Uberseder,[1] and M. Wiescher[1]

[1]*Department of Physics, University of Notre Dame, Notre Dame, Indiana 46556, USA*
[2]*Università degli Studi di Napoli "Frederico II" and INFN, Napoli, Italy*
[3]*Laboratori Nazionali del Gran Sasso (LNGS), INFN, Assergi (AQ), Italy*
[4]*Department of Physics, University of Toronto, Toronto, Ontario M55 1A7, Canada*
[5]*Forschungszentrum Dresden, Rossendorf, Dresden, Germany*
[6]*INFN, Padova, Italy*
[7]*Universitá degli Studi di Padova and INFN, Padova, Italy*
[8]*Universitá degli Studi di Genova and INFN, Genova, Italy*
[9]*Institute of Nuclear Research (ATOMKI), Debrecen, Hungary*
[10]*Max-Planck-Institut für Chemie, Mainz, Germany*
[11]*Universitá degli Studi di Torino and INFN, Torino, Italy*
[12]*Università degli Studi di Milano and INFN, Sezzione di Milano, Milan, Italy*
[13]*Institut für Kernphysik, Forschungszentrum Karlsruhe, Karlsruhe, Germany*
[14]*Institute für Experimentalphysik III, Ruhr-Universität Bochum, Bochum, Germany*
[15]*Institut für Materialforschung I, Forschungszentrum Karlsruhe, Karlsruhe, Germany*
[16]*Osservatorio Astronomico di Collurania, Teramo, and INFN Napoli, Italy*
[17]*Seconda Università di Napoli, Caserta, and INFN, Napoli, Italy*

(Received 16 June 2010; published 12 November 2010)

The ^{15}N$(p,\gamma)^{16}$O reaction represents a breakout reaction linking the first and second cycles of the CNO cycles redistributing the carbon and nitrogen abundances into the oxygen range. The reaction is dominated by two broad resonances, at $E_p = 338$ and 1028 keV, and a direct capture contribution to the ground state of ^{16}O. Interference effects between these contributions both in the low-energy region ($E_p < 338$ keV) and between the two resonances ($338 < E_p < 1028$ keV) can dramatically affect the extrapolation to energies of astrophysical interest. To facilitate a reliable extrapolation, the ^{15}N$(p,\gamma)^{16}$O reaction has been remeasured covering the energy range from $E_p = 1800$ keV down to 130 keV. The results have been analyzed in the framework of a multilevel R-matrix theory and an $S(0)$ value of 39.6 keV b has been found.

DOI: 10.1103/PhysRevC.82.055804 PACS number(s): 26.20.Cd, 25.40.Lw

I. INTRODUCTION

The energy production and nucleosynthesis in stars are characterized by nuclear reaction sequences that determine the subsequent phases of stellar evolution. Energy production during the first hydrogen burning phase takes place through the fusion of four protons into helium. This occurs through either *pp* chains or CNO cycles. The *pp* chains dominate hydrogen burning in first-generation stars with primordial abundance distributions and in low-mass stars, $M \leqslant 1.5M_{\odot}$. CNO cycles dominate energy production in more massive, $M \geqslant 1.5M_{\odot}$, second- or later-generation stars with an appreciable abundance of CNO isotopes. CNO cycles are characterized by sequences of radiative capture reactions and β-decay processes as shown in Fig. 1.

At stellar temperatures the ^{14}N$(p,\gamma)^{15}$O reaction is the slowest process in the cycle, defining the time scale and the overall energy production rate [2–4]. This reaction is therefore of importance for the interpretation of CNO burning. The proton capture by ^{15}N is relevant, as it is a branch point linking the first CNO or CN cycle with the second CNO or NO cycle, as shown in Fig. 1 [5]. This branching has always been a matter of debate, as both reactions are characterized by strong, low-energy resonances.

The reaction rate of ^{15}N$(p,\alpha)^{12}$C is determined by two broad, low-energy, s-wave resonances, at $E_p = 338$ and 1028 keV, populating the $J^{\pi} = 1^-$ states at 12.44 and 13.09 MeV, respectively, in the ^{16}O compound nucleus. There have been a number of low-energy measurements [6–8], which provide the basis for the present rate in the literature [9,10]. Recently, three lower-energy points were derived from an indirect "Trojan horse method" [11], which are consistent with low-energy data [6–8].

The competing ^{15}N(p,γ^{16})O reaction decays predominately to the ground state of ^{16}O and exhibits the same two resonances but, in addition, is expected to have a strong nonresonant direct capture component [12]. The presently

*leblanc.pj@gmail.com

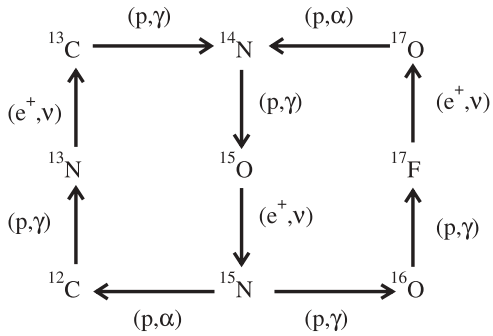

FIG. 1. Diagram of the CNO bi-cycle [1].

available low-energy cross-section data from Refs. [12–14], and differ substantially at lower energies. This poses difficulties for a reliable extrapolation of the cross section toward the stellar energy range. An extrapolation was performed [12] using a two-level Breit-Wigner formalism taking into account the direct capture contribution. The present reaction rate for ^{15}N$(p,\gamma)^{16}$O [10] relies entirely on the predictions of Ref. [12].

To reduce the uncertainty in the strength of the direct capture term, single-particle transfer reactions have been performed [15] to determine the proton asymptotic normalization coefficient (ANC) for the ground state of ^{16}O. With this ANC value $C^2_{p_{1/2}} = (192 \pm 26)$ fm^{-1}, R-matrix fits to the ^{15}N$(p,\gamma)^{16}$O data have been performed [15], which resulted in smaller values for the low-energy cross section than those obtained in Ref. [12]. This result was confirmed by an independent R-matrix analysis of the existing data [16]. This conclusion was, furthermore, supported by a study in which both the (p,α) and the (p,γ) reactions were analyzed simultaneously with a multilevel, multichannel R-matrix formalism [17].

Low-energy data points were extracted from a reanalysis [18] of a study of ^{14}N$(p,\gamma)^{15}$O performed at the LUNA underground accelerator facility at the Gran Sasso laboratory. This experiment was performed using a windowless, differentially pumped gas target with natural nitrogen gas. To detect the γ-ray signal, a large BGO scintillator detector was used to observe the characteristic γ decay in summing mode [19]. Because the natural abundance of ^{15}N is low, the yield of the ^{15}N(p,γ) signal was weak and overshadowed by the beam-induced background yield from proton capture reactions on target impurities and from the ^{14}N(p,γ) reaction. The measurements were therefore limited to energies below 230 keV. The proposed cross section results are clearly lower than the values obtained in Ref. [12] but also slightly lower than the results in Refs. [13] and [14]. Given the strong background conditions, the results could not be normalized to the known on-resonance yield at 338 keV and systematic errors in the data cannot be excluded.

Because of the inconsistencies in the existing data and the uncertainties of an R-matrix analysis based on these existing data, we have performed a new study of the ^{15}N$(p,\gamma)^{16}$O over a wide energy range using high-resolution Ge detectors. In Sec. II the experimental approach at the Notre Dame Nuclear Science Laboratory (NSL) and the LUNA II facility at the Gran Sasso underground laboratory is discussed. This is followed by a discussion of the experimental data in Sec. III. In Sec. IV the stellar nuclear reaction rate based on the present data is calculated and compared with existing results.

II. EXPERIMENTAL SETUP

A. Accelerators and experimental setup

The experiment was performed at two separate facilities. At the University of Notre Dame the 4-MV KN Van de Graaff accelerator provided proton beams in an energy range of 700 to 1800 keV with beam intensities limited to $\leqslant$10 μA on the target because of the high count rate in the Ge detector from the ^{15}N$(p,\alpha_1\gamma)^{12}$C reaction. The energy calibration of this machine was established to better than 1 keV using the well-known ^{27}Al$(p,\gamma)^{28}$Si resonance at 992 keV [19]. The 1-MV JN Van de Graaff accelerator at Notre Dame was used in the range of 285 to 700 keV with proton beams of 20 μA. The energy of this machine was calibrated using the well-known ^{15}N$(p,\alpha_1\gamma)^{12}$C resonance at 429 keV [20].

The LUNA II facility [21], located at the Gran Sasso National Laboratory, uses a high-current, 400- kV, Cockroft-Walton–type accelerator. The accelerator provided proton beam currents on the target of up to 200 μA in the energy range 130 to 400 keV. In addition to the high beam output, the accelerator is extremely stable, and the voltage is known to an accuracy of about 300 eV.

The experimental setup in both experiments was very similar. The targets were water-cooled and mounted at 45° with respect to the beam direction. At Notre Dame the position of the beam on the target was defined by a set of vertical and horizontal slits. The beam was swept horizontally and vertically across a target area of 1 cm^2 by steerers to dissipate power over a large target area. At LUNA the ion beam optics provided a defocused beam on the target and no beam sweeping was applied. To avoid the buildup of impurities on the target, a Cu finger, cooled to LN_2 temperatures, was placed along the inside of the beamline extending as close to the target as possible. In addition, a bias voltage of about $-$400 V was applied to the isolated cold finger to suppress the secondary electrons ejected from the target owing to proton bombardment.

B. Targets

The Ti^{15}N targets were fabricated at the Forschungszentrum Karlsruhe by reactive sputtering of Ti in a nitrogen atmosphere enriched in ^{15}N to 99.95%. The stoichiometry was analyzed using Auger electron spectroscopy to confirm the composition. This test was performed on two target spots, one that had been exposed to a beam and one that was not exposed. The results agreed within $\leqslant$2% with the nominal stoichiometry of 1:1. Isotopic abundances were experimentally verified by comparing the yield of the 278-keV ^{14}N$(p,\gamma)^{15}$O resonance [3] from the enriched targets with that obtained using a target produced with a natural nitrogen gas. The results of this measurement showed an abundance of $\leqslant$2% ^{14}N for the thin targets, corresponding to a ^{15}N enrichment of $\geqslant$98%, in agreement with the quote of the supplier. For the thick target used at LUNA, ^{14}N and ^{15}N enrichment of 17.4% $\pm$ 2.0%

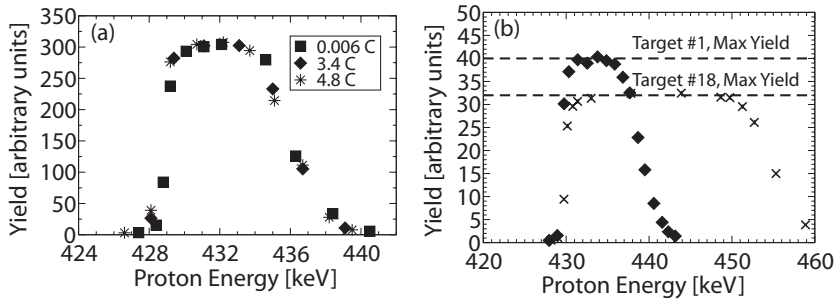

FIG. 2. Left: Notre Dame target has a measured width of approximately 7.2 keV at E_p = 430 keV. Squares, diamonds, and stars correspond to 0.006, 3.4, and 4.8 C of accumulated charge on the target, respectively. Right: LUNA thin (diamonds) and thick (crosses) targets have measured widths of ∼9.5 and ∼25 keV, respectively. The difference in stoichiometry between the two targets can be seen by comparing the plateau heights from the same resonance scan of each target (right).

and 82.6% ± 2.0% were found, respectively, most likely caused by a contamination of the enriched gas during sputtering.

The thicknesses of all TiN targets were measured using the narrow ^{15}N(p,$\alpha_1\gamma$)^{12}C resonance at 429 keV [20]. The target used at Notre Dame had a thickness of 7.2 ± 0.3 keV at E_p = 429 keV and the two targets used at LUNA had thicknesses of 9.5 ± 0.4 and 24.8 ± 0.5 keV at E_p = 429 keV, respectively. The stability of the Notre Dame targets was checked continuously during the course of the experiment using the ^{15}N(p,$\alpha_1\gamma$)^{12}C resonance. The thin LUNA target was monitored by rescanning the top of the 338-keV resonance in ^{15}N(p,γ)^{16}O. The thick LUNA target could also be monitored using the ^{14}N(p,γ)^{15}O resonance at E_p = 278 keV because of the high ^{14}N content (17%) of this target. Because of the relatively low power density delivered at Notre Dame, the target saw virtually no degradation over the experiment with an accumulated charge of 5 C (see Fig. 2), and no yield corrections were necessary. During the LUNA experiment with significantly higher beam currents, the thickness of the thin target was reduced by 27% after an accumulated charge of 17 C, and that of the thick target by 30% after an accumulated charge of 65 C (see Fig. 3).

C. Detectors

At the NSL, the γ rays were observed using a HPGe clover detector, which consists of four HPGe crystals contained in the same cryostat. This unique arrangement allows the separate detectors to be used in the so-called add-back mode [22]. At

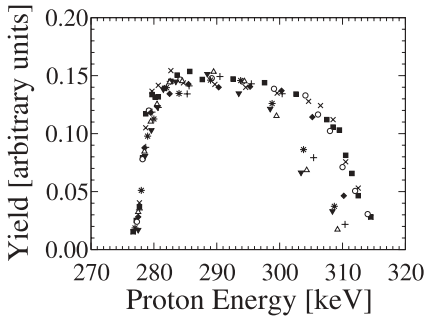

FIG. 3. Targets scans of the thick target [18] using the ^{14}N(p,γ)^{15}O, E_p = 278 keV resonance. The target was stable until about 20 C and went through significant deterioration. Squares represent the initial target scan, while downward triangles represent the scan after 65 C on the target.

LUNA, a single-crystal, 115% HPGe detector from Bochum, Germany, was used for the detection of γ rays. Several sample spectra are shown in Fig. 4.

The primary advantage of the LUNA II facility is the low-background environment created by the rock cover from the Gran Sasso mountains. The rock acts as a shield from cosmic rays and therefore decreases the γ-induced background from cosmic rays in the detector and has been shown [23] to suppress the E_γ > 3.5 MeV background count rate in a Ge detector by 3 orders of magnitude. In each experiment the detectors were set up at an angle of 45° with respect to the beam direction, allowing the position of the detector to be set as close

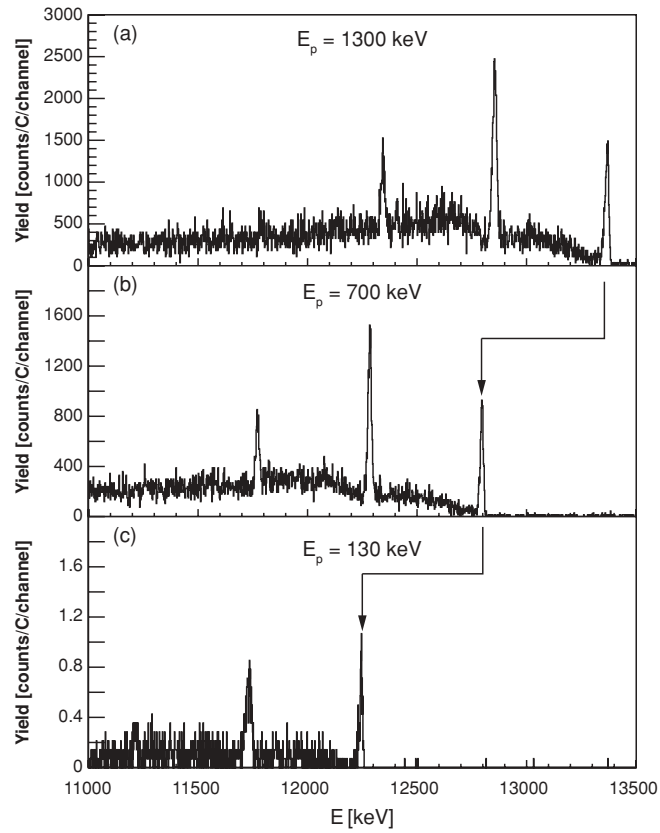

FIG. 4. Several sample spectra from the present ^{15}N(p,γ)^{16}O experiment. Spectra were taken with Notre Dame's KN accelerator (E_p = 1300 keV; top), Notre Dame's JN accelerator (E_p = 700 keV; middle), and the LUNA II accelerator (E_p = 130 keV; bottom). The ^{15}N(p,γ)^{16}O ground-state transition γ-ray peak is indicated in each spectrum by an arrow.

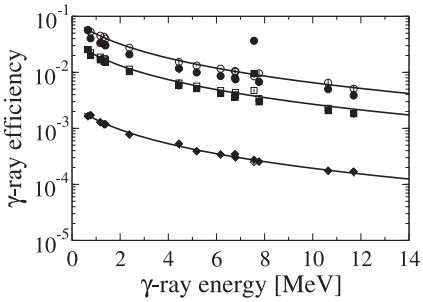

FIG. 5. Efficiency curves obtained at LUNA. Circles represent measurements at a distance of 1 cm; squares, at 3 cm; and diamonds, at 20 cm. Filled symbols represent data without summing corrections; open symbols include summing corrections.

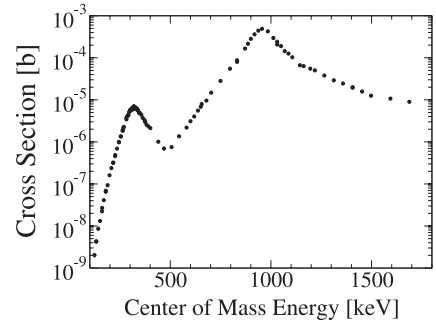

FIG. 6. Cross section for the ground-state transition of the $^{15}N(p,\gamma_0)^{16}O$ reaction versus the center-of-mass energy.

as possible to the reaction position. The relative efficiency of the γ-ray detector systems was measured using radioactive sources along with well-known capture γ reactions. At Notre Dame the relative efficiencies for high-energy γ rays were established using the $^{27}Al(p,\gamma)^{28}Si$ resonances at 992 keV [19] and 1183 keV [24] and the $^{23}Na(p,\gamma)^{24}Mg$ resonance at 1318 keV [25]. The efficiency was extended to a γ energy of 12.79 MeV using the $^{11}B(p,\gamma)^{12}C$ reaction at 675 and 1388 keV following the method of Ref. [25]. At LUNA the higher-energy efficiencies were determined using the 278-keV resonance in $^{14}N(p,\gamma)^{15}O$ [3] and the 163-keV resonance in $^{11}B(p,\gamma)^{12}C$ [20]. The ^{11}B resonance has a small angular distribution [26], and the correction for the relative intensity is less than 3%.

While summing is not of concern for the ground-state transition of the $^{15}N(p,\gamma)^{16}O$ reaction itself, summing plays a significant role in the determination of the γ efficiency. For this reason, the efficiency measurements at both laboratories were carried out at several detector-target distances and the data were simultaneously fitted for all distances following the procedure described by Imbriani *et al.* [3] (see Fig. 5). For the 1- and 5-cm measurements, there is one point that has significant summing corrections. This point corresponds to the ground-state transition in the $E_p = 278$ keV $^{14}N(p,\gamma)^{15}O$ reaction. While the ground-state transition of this reaction has a low branching ratio, each of the other cascades has significant probabilities, which lead to strong summing effects [3].

III. EXPERIMENTAL RESULTS

A. Cross-section determination

The excitation function for the ground-state transition of the reaction $^{15}N(p,\gamma)^{16}O$ has been measured in the energy range 131 to 1800 keV. It consists of three distinct, overlapping sections, LUNA data from 131 to 400 keV, JN data from 285 to 700 keV, and KN data from 700 to 1800 keV. The experimental yield Y (number of reactions per projectile) at proton energy E_p corresponds to the cross section $\sigma(E)$ integrated over the target thickness Δ,

$$Y(E_p) = \int_{E_p-\Delta}^{E_p} \frac{\sigma(E)}{\epsilon(E)} dE = \sigma(E_p) \int_{E_p-\Delta}^{E_p} \frac{f(E)}{\epsilon(E)} dE, \qquad (1)$$

where ϵ is the stopping power [27], and $f(E)$ represents the energy dependence of the cross section in the integration interval,

$$\sigma(E) = \sigma(E_p) f(E), \qquad (2)$$

with $\sigma(E_p)$ the cross section at E_p. This reduces to the well-known thin-target yield equation if the cross section is constant over the target thickness, $f(E) = 1$. However, at energies where the cross section varies significantly over the target thickness, the yield has to be corrected to extract the cross section. This correction factor is given by

$$1 \Big/ \int_{E_p-\Delta}^{E_p} \frac{f(E)}{\epsilon(E)} dE \qquad (3)$$

and requires the knowledge of the energy dependence of the cross section in the energy interval Δ, $f(E)$. This problem can be solved by an iterative method. In the first step $f(E) = 1$ is assumed, resulting in an approximation of the cross section, which in turn can be used to calculate a new correction factor. This process is continued until no change in the resulting cross section is obtained. This process quickly converges after two or three iterations. The resulting cross section is shown in Fig. 6.

An alternative method for determining the cross section was used, in which the data were analyzed following the approach described in Ref. [3]. Here, a brief review of the method is given, which consists of the analysis of the shape of the γ line.

The cross section, the stopping power of protons in TiN, the γ-ray efficiency, and the detector resolution all have an influence on the γ-ray line shape observed in a spectrum. The observed energy of the γ ray is related to the proton energy by [1]

$$E_\gamma = E_p \frac{M}{M+m} + Q - E_x - \Delta E_{\mathrm{Rec}} + \Delta E_{\mathrm{Dop}}. \qquad (4)$$

The number of counts N_i in channel i of the γ spectrum, corresponding to the energy bin $E_{\gamma i}$ to $E_{\gamma i} + \delta E_\gamma$ (δE = dispersion in units of kiloelectronvolts per channel) is given by the expression

$$N_i = \frac{\sigma(E_{pi}) \delta E_\gamma \eta_{fep}(E_{\gamma i}) b_j}{\epsilon(E_{pi})} \qquad (5)$$

for $E_{pi} \leqslant E_p$ (E_{pi} = proton energy corresponding to channel i, E_p = incident proton energy), where $\sigma(E_{pi})$ is the capture cross section, $\eta_{fep}(E_{\gamma i})$ is the γ-ray detection efficiency,

$\epsilon(E_{pi})$ is the stopping power, and b_j is the branching of the associated decay. The conversion from $E_{\gamma i}$ to E_{pi} includes the Doppler and recoil effects. The result is folded with the known detector resolution ΔE_γ to obtain the experimental line shape.

Finally, to infer the cross section in the energy window defined by the target thickness, the cross section was written as the sum of two resonance terms and a constant, nonresonant term as described in Ref. [28]. In these fits, the free parameters were the nonresonant astrophysical S factor and the γ-ray background parameters. The results of both methods are in excellent agreement.

The absolute cross section for the ^{15}N$(p,\gamma)^{16}$O reaction was measured on top of the two broad resonances at proton energies of 338 and 1028 keV using two independent well-known reaction standards and two independent methods. All measurements were performed at three distances ($d = 1$, 5, and 20 cm) to check for systematic errors. The exception to this protocol was the ^{15}N$(p,\gamma)^{16}$O measurement at $E_p = 338$ keV, where the yield at 20 cm was too low. In the first method the cross sections were determined relative to the thick-target yield $Y_\infty(^{27}\mathrm{Al})$ of the well-known ^{27}Al$(p,\gamma)^{28}$Si resonance at 992 keV,

$$Y_\infty(^{27}\mathrm{Al}) = \frac{\lambda^2(E_R)}{2\epsilon(E_R)}\frac{M+m}{M}\omega\gamma_R, \tag{6}$$

with $m(M)$ the mass of the projectile(target), λ the DeBroglie resonance wavelength, and $\omega\gamma_R$ the resonance strength. Adopting the resonance strength of 1.93 ± 0.13 eV from Refs. [19], [29], and [30], the cross-section values of $\sigma_{338} = 6.7 \pm 0.6$ μb and $\sigma_{1028} = 446 \pm 40$ μb are obtained. The errors include the statistical error ($\leqslant$3%), the error in the relative efficiency (2%), the error in the relative charge measurement (2%), the uncertainty in stopping power values (5%), and the uncertainty of 7% arising from the reference resonance strength of ^{27}Al.

In the second method the cross sections were determined relative to the well-known 429-keV resonance in ^{15}N$(p,\alpha_1\gamma)^{12}$C [20]. In this case the cross section was calculated relative to the integral over the yield curve of the reference resonance, A^{ref}. The resonance strength $\omega\gamma$ is related to A^{ref} by

$$\omega\gamma = \frac{2}{\lambda^2}\frac{1}{n_t}A^{\mathrm{ref}}, \tag{7}$$

with n_t the number of target atoms per square centimeter, which can be calculated from the measured target thickness and the stopping power values. Using this relationship for A^{ref} [Eq. (7)], along with Eq. (6) and the thin-target yield approximation for the ^{15}N$(p,\gamma)^{16}$O reaction, the following formula can be derived:

$$\sigma_{(p,\gamma)}(E_p) = \left(\frac{\lambda^2(E_R)}{2}\right)\left(\frac{M+m}{M}\right)\left(\frac{\eta(4.4\ \mathrm{MeV})}{\eta(12\ \mathrm{MeV})}\right) \times \left(\frac{Y(E_p)}{A^{\mathrm{ref}}}\right)\omega\gamma_R, \tag{8}$$

with η the relative γ-ray efficiency. In this approach the result is independent of all target uncertainties. The yield of the 4.4-MeV γ rays from the ^{15}N$(p,\alpha_1\gamma)^{12}$C was corrected for the well-known angular distribution [31,32]. Using the resonance strength of $\omega\gamma_R = 21.2 \pm 1.4$ eV from Ref. [33], values of $\sigma_{338} = 6.4 \pm 0.6$ μb and $\sigma_{1028} = 436 \pm 44$ μb are obtained. The errors include the statistical error ($\leqslant$3%), the error of the relative efficiency (2%), the error of the relative charge measurement (2%), the error of A^{ref} owing to the numerical integration and angular distribution correction (6%), and the uncertainty of 7% in the reference value [33].

TABLE I. Summary of present resonance cross sections in comparison to previous results.

E_R (keV)	Present study (μb)	Rolfs and Rodney [12] (μb)	Brochard *et al.* [14] (μb)	Hebbard [13] (μb)
338	6.5 ± 0.3	9.6 ± 1.3	6.3[a]	6.5 ± 0.3[b]
1028	438 ± 16	420 ± 60	490[a]	–

[a]No uncertainty is given.
[b]Error derived from a given reproducibility of 5%.

The weighted average of the results from the two methods gives final values of $\sigma_{338} = (6.5 \pm 0.3)$ μb (5%) and $\sigma_{1028} = (438 \pm 16)$ μb (4%) taking into account common error sources. The present results are compared to previous values [12–14] in Table I and are in very good agreement. An exception is the cross section at 338 keV from Ref. [12], which is about 50% higher than the other values. This discrepancy is discussed in more detail in the next section. Data from LUNA and the Notre Dame JN accelerators were normalized to the low-energy resonance, while data from the Notre Dame KN accelerator were normalized to the higher-energy resonance. Good agreement between the data sets was found at overlapping energies of about 700 keV.

B. Branching ratios

In previous experiments small cascade transitions have been observed for the broad resonances at 338 and 1028 keV [20]. For the 338-keV resonance a branching ratio of (1.2 ± 0.1)% for the transition to the 6050-keV level was found, in good agreement with the literature value of $1.2\% \pm 0.4\%$ [20]. For the 1028-keV resonance, branches to the 6050-keV level (1.0 ± 0.3)% and to the 7118-keV level (2.8 ± 0.3)% were measured and were also in good agreement with the literature values of (1.4 ± 0.4)% and (3.1 ± 0.8)%, respectively [20].

C. Angular distributions

In previous analyses of the ^{15}N$(p,\gamma_0)^{16}$O reaction [12,15,16], a direct capture component was required to fit the data. In each of these cases, only the $l_i = 0$ initial wave was included in the calculation. This component represents s-wave capture and, therefore, interferes with the resonant component of the cross section. The s-wave components yield isotropic γ-ray distributions [12,28]. However, an $l_i = 2$ direct capture component is allowed for $E1$ transitions and can contribute to the reaction, possibly introducing some anisotropy in the γ decay. In looking for this signature, the setup was tested using the 1-MeV resonance, which is reported to be isotropic [12]. Measurements were made with the central clover axis at

several angles relative to the beam direction, with a nominal distance of 5 cm. To extract additional data points, the add-back feature was used to treat the left and right halves of the clover system as separate detectors, where Monte Carlo calculations using the code GEANT4 [34] yielded an effective angular offset of each half from the central detector axis of 15°. Measurements with a calibrated ^{137}Cs source and the isotropic 278-keV resonance of ^{14}N$(p,\gamma)^{15}$O made corrections to the absorption effects possible. The results confirmed the isotropy of the angular distribution of the ground-state decay γ rays from the 1028-keV resonance in ^{15}N$(p,\gamma_0)^{16}$O.

In the search for the $l_f = 2$ component, angular distribution measurements of ^{15}N$(p,\gamma_0)^{16}$O were made at a proton energy of 540 keV at detection angles of 0°, 45°, and 90° relative to the beam axis. With two clover segments, this resulted in six data points. Two of these points were excluded owing to large absorption effects from the shape of the target chamber. The resulting angular distribution was fit with a function of the form $W(\theta) = a_0^{\rm exp} + a_2^{\rm exp} P_2(\cos\theta)$, where P_2 is the $L = 2$ Legendre polynomial, and $a_2^{\rm exp} = Q_2 a_2$, where Q_2 is the usual geometrical correction factor owing to the finite size of the detector [35]. The Q_2 term can be directly determined using the ^{16}O(p,γ) DC $\rightarrow$ 495 keV reaction [28]. This reaction has a well-known angular distribution of the form $W(\theta) = \sin^2(\theta)$. Plotting the measured $W(\theta)$ with respect to $\sin^2(\theta)$, the deviation of the slope from 1.0 gives directly the Q_2 value. Using the left and right clover halves to measure the ^{16}O$(p,\gamma)^{17}$F DC $\rightarrow$ 495 keV, a value of $Q_2 = 0.975 \pm 0.020$ was found. This results in an a_2 value for the ^{15}N$(p,\gamma_0)^{16}$O reaction at 540 keV of 0.08 ± 0.10, which is consistent with isotropy.

IV. *R*-MATRIX ANALYSIS

An *R*-matrix analysis was performed, which mirrored the procedure in previous analyses [12,15,16]. This analysis included the two broad 1^- resonance levels and a direct capture contribution. The analysis was performed with the multichannel *R*-matrix code AZURE [36]. Details of the theory and the nomenclature are given in Ref. [36] and references therein. The best-fit results are shown in Fig. 7, where the cross sections have been converted to the astrophysical *S* factor. This fit results in an $S(0)$ value of 39.6 keV b.

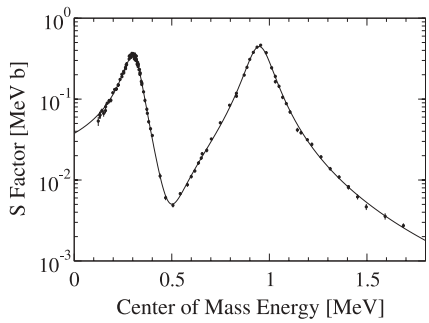

FIG. 7. Experimental *S* factor for the ground-state transition of the ^{15}N$(p,\gamma_0)^{16}$O reaction shown together with the best-fit results of an *R*-matrix calculation using the code AZURE.

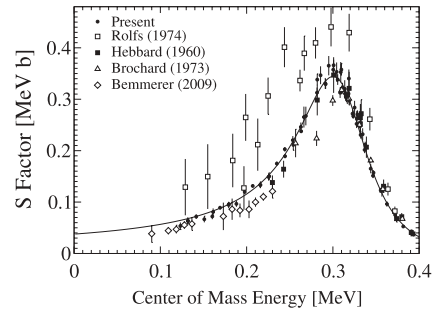

FIG. 8. Low-energy region of the present data set (filled circles) shown with AZURE *R*-matrix calculation along with previous measurements by Rolfs and Rodney (open squares) [12], Hebbard (filled squares) [13], Brochard *et al.* (open triangles) [14], and Bemmerer *et al.* (open diamonds) [18] in the region of 0–400 keV.

Looking closer at the low-energy region (see Fig. 8) and comparing the results with those of previous experiments, the low-energy data from Ref. [12] are inconsistent with the present results. While this data set agrees very well at higher energies, it starts to deviate below a proton energy of 400 keV. There is no obvious reason for this inconsistency but it should be noted that the low-energy data of Rolfs and Rodney [12] carry a significant uncertainty in this region. The data of Hebbard [13] are in reasonably good agreement above 230 keV. The data of Brochard *et al.* [14] show good agreement except for the three data points below the 338-keV resonance, which show a large scatter. The recent Bemmerer *et al.* data [18] are systematically lower than the present data and, also, seem to have a slightly different energy dependence.

The parameters for the best fit are listed in Table II. With the exception of the first resonance, most parameters are in fair agreement with previous results [15,16]. The width of the first resonance is dominated by the α width [20]. This parameter is, therefore, well constrained by the present (p,γ) data. The resonance strength, however, is determined by the product of the proton and the γ width. Without including proton scattering data in the fit, these parameters are not well constrained. However, it should be noted that tests showed that this ambiguity has no influence on the extrapolation of the data. In these tests, the proton width (γ_{p_1}) was fixed at different values while allowing the other parameters to vary. For the higher-energy resonance the proton and α width are comparable, which provides more of a constraint on the parameters. In addition, the present result for the ground-state ANC is significantly larger than the value in Ref. [15], which cannot be attributed to the choice of radius (see the following). While these differences do not have an impact on the extrapolation of the *S* factor to lower energies, a more thorough analysis is warranted for interpretation of the *R*-matrix parameters. This will be addressed in a forthcoming publication [37], where the results of simultaneous multichannel fits to all relevant reaction channels will be presented.

In the present parameter space the only non-*s*-wave contribution arises from the *d*-wave component of the direct capture. Using the parameters for the best fit, the γ-ray angular distribution was calculated at the minimum of the cross section between the two resonances at 540 keV, yielding a value of

TABLE II. Best-fit R-matrix parameters for the ^{15}N$(p,\gamma)^{16}$O reaction (E_x in MeV, γ_i^2 in keV). Channel radii of $a_p = 5.030$ fm and $a_\alpha = 6.500$ fm were used in the fit. The boundary condition (BC) in the fit was chosen to be equal to the shift function at the energy of the lowest $J^\pi = 1^-$ resonance. Because of this choice of BC, the Γ_{γ_1} (in eV) can be calculated directly from the reduced width amplitude, while Γ_{γ_2} is calculated from the Barker transformation of the reduced width amplitude [36]. The parameters listed here are mainly intended to enable the reader to reproduce the fit presented in this article, and should not be regarded as final. With respect to the physical interpretation of these fit parameters, a detailed discussion will be presented in a forthcoming paper [37].

Reference	E_1, $J^\pi = l^-$	$\gamma^2_{p_1}$, $l_p = 0$	$\gamma^2_{\alpha_{01}}$, $l_\alpha = 1$	$\gamma^2_{\gamma_1}$(int)	Γ_{γ_1}	E_2, $J^\pi = l^-$	$\gamma^2_{p_2}$, $l_p = 0$	$\gamma^2_{\alpha_{02}}$, $l_\alpha = 1$	$\gamma^2_{\gamma_2}$(int)	Γ_{γ_2}	$C_{\text{g.s}}$ (fm$^{1/2}$), $s, d \to p$	$\theta_{\text{g.s}}$
Present	12.438	52.8	13.5	51.3	33.8	13.087	309.1	5.0	34.1	38.7	23.22	0.608
[15]	12.439	280.9	12.5	–	8.8 ± 1.5	13.089	271.4	6.1	–	50 ± 8	13.85	–
[16, RR]	12.452	93.6	13.5	38.0	–	13.111	416.0	0.812	0.5	–	–	1.944
[16, HH]	12.447	355.2	10.6	7.2	–	13.087	265.2	5.4	56.2	–	–	0.569

$a_2 = 0.034$. The result is consistent with the experimental upper limit of 0.18 (see Sec. III C).

The sensitivity of the best fit was tested against several key parameters. In multiparameter fitting, uncertainties of specific parameters are determined in terms of confidence regions. For a nine-parameter fit (E_λ, γ_i for both levels plus ANC or $\theta_{\text{g.s.}}$), a 70% confidence region for one of the parameters is defined by the range where $\chi^2 \leqslant \chi^2_{\text{min}} + 10$ [38]. The degrees of freedom is 102 (113 data points, 9 parameters), resulting in a reduced χ^2 of 1.8.

Radii of $r_p = 5.03$ fm and $r_\alpha = 6.5$ fm were taken from Ref. [16]. The dependence of the fit on the proton radius was tested, and the results are shown in Fig. 9(a). Any proton radius value between 4 and 6 fm is considered acceptable. Variation of the radius over this range corresponds to only a 5% uncertainty in the $S(0)$ extrapolation. This test also showed that the ANC is not very sensitive to the choice of the radius. The best fit gives a ground-state ANC of (23 ± 3) fm$^{-1/2}$ (corresponding to a reduced width amplitude of $\theta_{\text{g.s.}} = 0.61$). The error associated with the ANC was determined by fixing the ANC at different values and finding a new best fit. The results of this procedure are shown in Fig. 9(b). Even though the results give a 13% uncertainty for the ANC, the variation in $S(0)$ owing to this procedure is only 4%.

To evaluate the uncertainty of the fit itself, fits were performed that were forced to result in different $S(0)$ values by inserting a fake data point at 1.5 keV with extremely small errors. The small error of this data point forces the calculation to match this fictitious data point and thus vary the extrapolation. By varying the fictitious point and observing the change in the χ^2_{tot}, the experimental uncertainty of the extrapolation can be determined (see Fig. 10). This results in an uncertainty of ± 0.6 keV b. Including the 5% error of the absolute cross section gives a final $S(0)$ value of (39.6 ± 2.6) keV b. This value is compared with previous extrapolations in Table III [12,13,15–17]. The present result is in good agreement with the original value of Hebbard [13], the Barker [16] analysis of the Hebbard data (labeled HH in

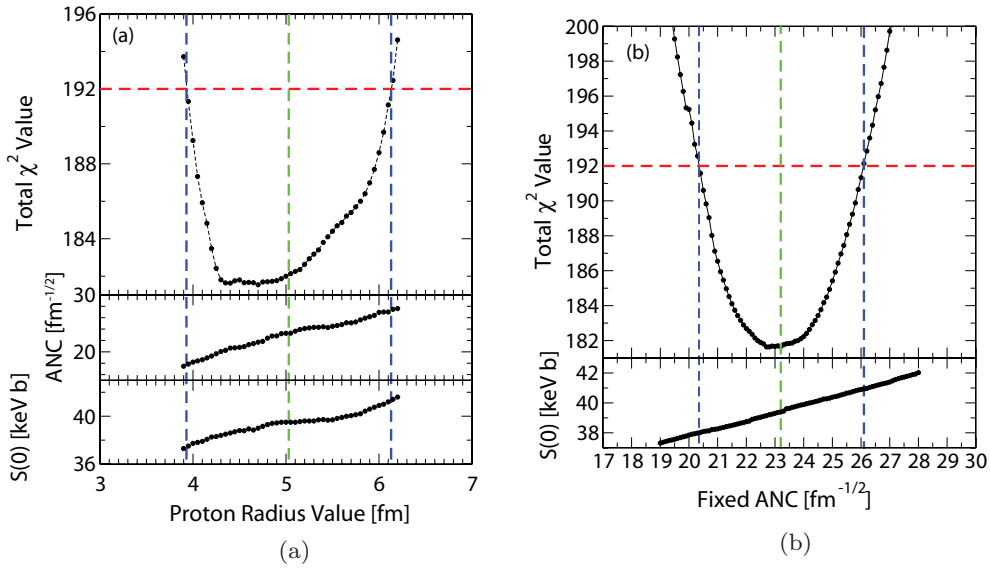

(a) (b)

FIG. 9. (Color online) Dependence of AZURE fits on key parameters used in the fits. Parameters were varied, noting that for a nine-parameter fit, a 70% confidence region is defined for $\approx\chi^2 = \chi^2_{\text{min}} + 10$ [38]. Even though a lower χ^2 was found with a radius of about 4.4 fm, 5.03 was chosen so as to be more comparable to the value in Ref. [16]. The ANC was found to be (23 ± 3) fm$^{-1/2}$. Fixing the ANC to the value in Ref. [15] gives a χ^2 that is much higher than the current best-fit value.

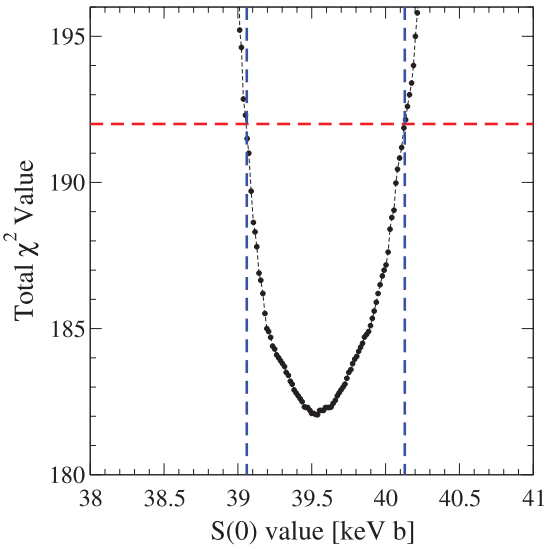

FIG. 10. (Color online) Variation of χ^2 with extrapolated S(0) values (for details, see text).

Table III, and the results of Mukhamedzhanov *et al.* [15]. The extrapolation of the Rolfs and Rodney data [12] (Rolfs and Rodney [12], Barker [16], and Simpson [17]; labeled RR in Table III) are all significantly higher because of the larger low-energy cross sections used for their fit analysis.

V. REACTION RATE

Using the results from the AZURE extrapolations, the reaction rates can be numerically determined using the formalism outlined in Ref. [10]:

$$N_A\langle\sigma v\rangle = 3.73\times10^7\mu^{-\frac{1}{2}}T^{-\frac{3}{2}} \times\int_0^\infty S(E)e^{(-2\pi\eta)}e^{(-11.605E/T)}dE, \quad (9)$$

with μ the reduced mass, T the temperature (in GK), and η the Sommerfeld parameter; the results are given as cubic centimeters per mole per second. The preceding function was numerically integrated for temperatures between $T = 0.01$ GK and $T = -10$ GK. The present data cover an energy range of $E = 0$ to 1.8 MeV, which validates the integration up to a temperature of $T = 1$ GK. For higher temperatures, the S-factor curve must be extended to energies higher than the present experimental data cover. We followed the procedure

TABLE III. Summary of previous results for extrapolated $S(0)$ values.

Analysis	$S(0)_\gamma$ (keV b)
Hebbard [13]	32
Rolfs and Rodney [12]	64 ± 6
Barker (RR) [16]	≈50–55
Barker (HH) [16]	≈35
Mukhamedzhanov *et al.* [15]	36.0 ± 6.0
Present study	39.6 ± 2.6

TABLE IV. Reaction rates for ^{15}N$(p,\gamma_0)^{16}$O. The present rates, along with the NACRE [10] and CA88 [9] results, are listed.

$T9$ (GK)	$N_A\langle\sigma v\rangle_{\text{Present}}$	$N_A\langle\sigma v\rangle_{\text{NACRE}}$ [10]	$N_A\langle\sigma v\rangle_{\text{CA88}}$ [9]
0.010	2.284×10^{-21}	4.33×10^{-21}	3.93×10^{-21}
0.015	1.377×10^{-17}	2.66×10^{-17}	2.34×10^{-17}
0.020	3.322×10^{-15}	6.50×10^{-15}	5.61×10^{-15}
0.030	3.215×10^{-12}	6.41×10^{-12}	5.38×10^{-12}
0.040	2.456×10^{-10}	4.96×10^{-10}	4.08×10^{-10}
0.050	5.378×10^{-9}	1.09×10^{-8}	8.90×10^{-9}
0.060	5.681×10^{-8}	1.16×10^{-7}	9.36×10^{-8}
0.070	3.747×10^{-7}	7.64×10^{-7}	6.14×10^{-7}
0.080	1.784×10^{-6}	3.63×10^{-6}	2.91×10^{-6}
0.090	6.699×10^{-6}	1.36×10^{-5}	1.08×10^{-5}
0.100	2.104×10^{-5}	4.23×10^{-5}	3.37×10^{-5}
0.150	1.280×10^{-3}	2.46×10^{-3}	1.92×10^{-3}
0.200	1.908×10^{-2}	3.52×10^{-2}	3.09×10^{-2}
0.300	6.143×10^{-1}	1.05×10^{0}	1.57×10^{0}
0.400	4.682×10^{0}	7.48×10^{0}	1.45×10^{1}
0.500	1.668×10^{1}	2.58×10^{1}	5.42×10^{1}
0.600	3.908×10^{1}	5.90×10^{1}	1.27×10^{2}
0.700	7.213×10^{1}	1.07×10^{2}	2.25×10^{2}
0.800	1.165×10^{2}	1.68×10^{2}	3.39×10^{2}
0.900	1.763×10^{2}	2.46×10^{2}	4.67×10^{2}
1.000	2.599×10^{2}	3.50×10^{2}	6.18×10^{2}
1.500	1.485×10^{3}	1.67×10^{3}	2.33×10^{3}
2.000	4.735×10^{3}	5.05×10^{3}	6.61×10^{3}
3.000	1.489×10^{4}	1.55×10^{4}	1.97×10^{4}
4.000	2.428×10^{4}	2.27×10^{4}	3.12×10^{4}
5.000	3.064×10^{4}	2.61×10^{4}	3.83×10^{4}
6.000	3.435×10^{4}	2.86×10^{4}	4.19×10^{4}
7.000	3.624×10^{4}	3.06×10^{4}	4.31×10^{4}
8.000	3.699×10^{4}	3.23×10^{4}	4.29×10^{4}
9.000	3.706×10^{4}	3.37×10^{4}	4.19×10^{4}
10.000	3.674×10^{4}	3.51×10^{4}	4.04×10^{4}

of the NACRE compilation [10], which handles this difficulty by equating all higher-energy S-factor values with the highest-energy data point, where the cross section varies only slowly with energy. The results are reeported in Table IV. At lower temperatures the present rate is lower than previous rates by up to a factor of 2, reflecting the change in the low-energy S factor.

Following the example of the NACRE compilations, the preceding results were fit using the following parametrization:

$$N_A\langle\sigma v\rangle = a_1 10^9 T^{-\frac{3}{2}}\exp[a_2T^{-\frac{1}{3}}-(T/a_3)^2][1+a_4T+a_5T^2] + a_6 10^3 T^{-\frac{3}{2}}\exp(a_7/T)+a_8 10^6 T^{-\frac{3}{2}}\exp(a_9/T), \quad (10)$$

where the best-fit parameters are given in Table V.

TABLE V. Best-fit parameters for the ^{15}N$(p,\gamma_0)^{16}$O reaction rate using the NACRE fitting formulations.

$a_1 = 0.523$	$a_4 = 6.339$	$a_7 = -2.913$
$a_2 = -15.240$	$a_5 = -2.164$	$a_8 = 3.048$
$a_3 = 0.866$	$a_6 = 0.738$	$a_9 = -9.884$

VI. CONCLUSION

The result of this work clearly demonstrates that there are significant uncertainties in the low-energy cross-section data of radiative capture processes of astrophysical relevance, despite many decades of low-energy reaction studies. These uncertainties directly affect our understanding and interpretation of solar and stellar hydrogen burning phenomena. In this case the new results influence primarily the leakage rate from the CN to the ON cycle in stellar burning via the ^{15}N$(p,\gamma)^{16}$O radiative capture process, which is reduced by a factor of 2 compared to the previous rate used traditionally in CNO nucleosynthesis simulations. In particular, the change in rate will modify the equilibrium abundance of ^{16}O, which is correlated with the leakage rate of ^{15}N$(p,\gamma)^{16}$O from the CN cycle and the rate of ^{16}O$(p,\gamma)^{17}$F in the NO cycle. However, a detailed study of the astrophysical impact of the present measurement goes beyond the aim of the present work but should benefit from recent studies of low-energy reaction rates [36].

The reliability of stellar reaction rates depends critically on the quality of the experimental cross-section data. Direct measurements of the reaction cross sections in the Gamow range of stellar burning have been successful in only a few cases of reactions between light nuclei. Considering the anticipated count rates for the CNO radiative capture reactions, we will continue to rely, for most cases, on the extrapolation of low-energy measurements into the Gamow range. The present analysis clearly demonstrates that this requires a twofold approach, pursuing the direct reaction measurements to the lowest possible energies in a background-shielded environment but, also, expanding the experimental range of the measurements to determine unambiguously the various reaction components of the radiative capture process. The latter step is essential for minimizing the uncertainties in the R-matrix analysis of the cross section and can be complemented by independent studies that explore independently the strength of specific "hidden" reaction components such as the direct capture through ANC measurements and analysis.

The approach taken here for study of the ^{15}N$(p,\gamma)^{16}$O reaction has succeeded in combining both the efforts of improving the extent and quality of the low-energy cross-section data in underground accelerator experiments. At the same time the study has improved on the detailed measurement of higher-energy data, providing a better constraint on determining the external capture component and its impact on the low-energy extrapolation of the reaction cross section. The combination of these two complementary measurements successfully reduced the overall uncertainty in the ^{15}N$(p,\gamma)^{16}$O reaction rate.

ACKNOWLEDGMENTS

We are extremely grateful for the help of the technical staff at both the Nuclear Science Laboratory at the University of Notre Dame and the Gran Sasso facility. R.E.A. thanks the NSERC for partial financial support through the DRAGON Grant at TRIUMF. This work was funded in part by National Science Foundation Grant No. 0758100 and Joint Institute for Nuclear Astrophysics Grant No. 0822648, along with INFN, Italy.

[1] C. E. Rolfs and W. S. Rodney, *Cauldrons in the Cosmos: Nuclear Astrophysics* (University of Chicago Press, Chicago, 1988).
[2] G. Imbriani *et al.*, Astron. Astrophys. **420**, 625 (2004).
[3] G. Imbriani *et al.*, Eur. Phys. J. A **25**, 455 (2005).
[4] R. C. Runkle, A. E. Champagne, C. Angulo, C. Fox, C. Iliadis, R. Longland, and J. Pollanen, Phys. Rev. Lett. **94**, 082503 (2005).
[5] G. R. Caughlan and W. A. Fowler, Astrophys. J. **136**, 453 (1962).
[6] A. Schardt, W. A. Fowler, and C. C. Lauritsen, Phys. Rev. **86**, 527 (1952).
[7] J. L. Zyskind and P. D. Parker, Nucl. Phys. A **320**, 404 (1979).
[8] A. Redder, H. W. Becker, H. Lorenz-Wirzba, C. Rolfs, P. Schmalbrock, and H. P. Trautvetter, Z. Phys. **305**, 325 (1982).
[9] G. R. Caughlan and W. A. Fowler, At. Data Nucl. Data Tables **40**, 283 (1988).
[10] C. Angulo *et al.*, Nucl. Phys. A **656**, 3 (1999).
[11] M. LaCognata, V. Z. Goldberg, A. M. Mukhamedzhanov, C. Spitaleri, and R. E. Tribble, Phys. Rev. C **80**, 012801 (2009).
[12] C. Rolfs and W. S. Rodney, Nucl. Phys. A **235**, 450 (1974).
[13] D. Hebbard, Nucl. Phys. **15**, 289 (1960).
[14] F. Brochard, P. Chevallier, D. Disdier, and F. Scheibling, J. Phys. **34**, 363 (1973).
[15] A. M. Mukhamedzhanov *et al.*, Phys. Rev. C **78**, 015804 (2008).
[16] F. C. Barker, Phys. Rev. C **78**, 044612 (2008).
[17] E. C. Simpson, Master's thesis, University of Surrey, 2006.
[18] D. Bemmerer *et al.*, J. Phys. G **36**, 045202 (2009).
[19] J. Keinonen and A. Anttila, Comment. Physico-Math. **46**, 61 (1976).
[20] F. Ajzenberg-Selove, Nucl. Phys. A **460**, 1 (1986).
[21] H. Costantini, A. Formicola, G. Imbriani, M. Junker, C. Rolfs, and F. Strieder, Rep. Prog. Phys. **72**, 086301 (2009).
[22] S. Dababneh, N. Patronis, P. A. Assimakopoulos, J. Görres, M. Heil, F. Käppeler, D. Karamanis, S. O'Brien, and R. Reifarth, Nucl. Instrum. Methods Phys. Res. A **517**, 230 (2004).
[23] D. Bemmerer *et al.*, Eur. Phys. J. A **24**, 313 (2005).
[24] M. A. Meyer, I. Venter, and D. Reitmann, Nucl. Phys. A **250**, 235 (1975).
[25] F. Zijderhand, F. P. Jansen, C. Alderliesten, and C. van der Leun, Nucl. Instrum. Methods Phys. Res. A **286**, 490 (1990).
[26] F. E. Cecil, F. J. Wilkinson, R. A. Ristinen, and R. Rieppo, Nucl. Instrum. Methods Phys. Res. A **234**, 479 (1985).
[27] J. F. Ziegler, *Particle Interaction with Matter*, [http://www.srim.org/] (2008).
[28] C. Rolfs, Nucl. Phys. A **217**, 29 (1973).
[29] B. M. Paine and D. G. Sargood, Nucl. Phys. A **331**, 389 (1979).
[30] A. Antilla, J. Keinonen, M. Hautala, and I. Forsblom, Nucl. Instrum. Methods **147**, 501 (1977).
[31] C. A. Barnes, D. B. James, and G. C. Neilson, Can. J. Phys. **30**, 717 (1952).
[32] A. A. Kraus, A. P. French, W. A. Fowler, and C. C. Lauritsen, Phys. Rev. **89**, 299 (1953).

[33] H. W. Becker *et al.*, Z. Phys. A **351**, 453 (1995).
[34] S. Agostinelli *et al.* (GEANT4 Collaboration), Nucl. Instrum. Methods Phys. Res. A **506**, 250 (2003).
[35] A. J. Ferguson, *Angular Correlation Methods in Gamma Ray Spectroscopy* (North-Holland, Amsterdam, 1965).
[36] R. E. Azuma *et al.*, Phys. Rev. C **81**, 045805 (2010).
[37] P. J. LeBlanc *et al.* (in press, 2010).
[38] F. James, *Minuit: Function Minimization and Error Analysis*, 94.1 ed. (CERN, 1994).